22. T. Kirschstein, W. Greffrath, D. Busselberg, R. D. Treede, *J. Neurophysiol.* **82**, 2853 (1999).
23. E. W. McCleskey and M. S. Gold, *Annu. Rev. Physiol.* **61**, 835 (1999).
24. I. Nagy and H. Rang, *Neuroscience* **88**, 995 (1999).
25. I. Nagy and H. P. Rang, *J. Neurosci.* **19**, 10647 (1999).
26. The VR1 gene was disrupted in JM1 mouse embryonic stem cells [M. Qui *et al.*, *Genes Dev.* **9**, 2523 (1995)]. See (*58*) for details of VR1-null mouse generation and northern blot analysis. All animal experiments were subject to institutional review and conducted in accordance with institutional guidelines.
27. The 100-kb VR1 genomic bacterial artificial chromosome clone was used as a fluorescence in situ hybridization probe on metaphase 129SV/J fibroblasts and mapped by comparison with centromere and telomere positions (Genome Systems, St. Louis, MO).
28. Immunohistochemistry was performed as described (*7*, *38*) with modifications. See (*58*) for details on immunohistochemistry and statistical analyses.
29. M. J. Caterina, T. A. Rosen, M. Tominaga, A. J. Brake, D. Julius, *Nature* **398**, 436 (1999).
30. Calcium imaging studies were performed on cultured dorsal root ganglion neurons as described (*5*, *29*) with modifications. See (*58*) for details.
31. M. J. Caterina *et al.*, data not shown.
32. See (*58*) for details on patch-clamp analysis of cultured sensory neurons.
33. Single cutaneous primary afferent neurons were recorded as described (*54*) [M. Kress, M. Koltzenburg, P. W. Reeh, H. O. Handwerker, *J. Neurophysiol.* **68**, 581 (1992)]. See (*58*) for details.
34. Nociceptor conduction velocities were as follows. C fibers: $VR1^{+/+}$, 0.56 ± 0.02; $VR1^{-/-}$, 0.58 ± 0.03; Aδ fibers: $VR1^{+/+}$, 5.2 ± 1.5; $VR1^{-/-}$, 6.4 ± 1.2 m/s.
35. Behavioral assays were performed as described (*40*, *59*) with modifications. See (*58*) for details.
36. Some residual paw swelling was observed with high doses (>1 μg) of capsaicin. This could, in principle, indicate the existence of a resiniferatoxin-insensitive, low-affinity capsaicin receptor but more likely reflects receptor-independent membrane perturbation effects similar to those previously reported with high-dose capsaicin [A. M. Feigin, E. V. Aaronov, B. P. Bryant, J. H. Teeter, J. G. Brand, *Neuroreport* **6**, 2134 (1995)]. Indeed, no significant swelling was seen with similarly effective concentrations of resiniferatoxin.
37. Individually housed adult mice, fed ad libitum, were fluid-restricted to a 3-hour test period per day. Fluid intake was monitored by weighing sipper bottles (Nalgene, Rochester, NY) containing the indicated solutions before and after the test period.
38. A. B. Malmberg, C. Chen, S. Tonegawa, A. I. Basbaum, *Science* **278**, 279 (1997).
39. Body temperature and locomotor activity were continuously monitored with intraperitoneal telemetric probes and VitaView Software (MiniMitter, Sun River, OR). One week after probe implantation, animals were injected subcutaneously on the back with capsaicin (1 mg/kg in 0.5 ml of 10% ethanol) or 10% ethanol alone.
40. A. Jancso-Gabor, J. Szolcsanyi, N. Jancso, *J. Physiol.* **206**, 495 (1970).
41. Median (and quartile range; qr) mechanical von Frey hair thresholds were as follows. C fibers: $VR1^{+/+}$, 8.0 qr 12.0; $VR1^{-/-}$, 8.0 qr 8.0; Aδ fibers: $VR1^{+/+}$, 5.6 qr 4.0; $VR1^{-/-}$, 8.0 qr 8.0 mN.
42. See (*58*) for details on spinal cord recording.
43. See (*58*) for details on analysis of heat-evoked spinal cord Fos immunoreactivity.
44. K. Hargreaves, R. Dubner, F. Brown, C. Flores, J. Joris, *Pain* **32**, 141 (1988).
45. H. O. Handwerker and P. W. Reeh, in *Proceedings of the VIth World Congress on Pain*, M. R. Bond, J. E. Charlton, C. J. Woolf, Eds. (Elsevier, Amsterdam, 1991), pp. 59–70.
46. M. E. Martenson, S. L. Ingram, T. K. Baumann, *Brain Res.* **651**, 143 (1994).
47. J. Levine and Y. Taiwo, in *Textbook of Pain*, P. D. Wall and R. Melzack, Eds. (Churchill Livingstone, Edinburgh, 1994), pp. 45–56.
48. Mustard oil (10% in mineral oil) was painted on both hind paws, and the hot plate assay was performed several minutes later.
49. CFA and nerve injury experiments were performed as described (*38*, *59*) with modifications. See (*58*) for details.
50. C. J. Benson, S. P. Eckert, E. W. McCleskey, *Circ. Res.* **84**, 921 (1999).
51. W. Jänig and J. F. Morrison, *Prog. Brain Res.* **67**, 87 (1986).
52. P. M. Zygmunt *et al.*, *Nature* **400**, 452 (1999).
53. W. J. Martin and A. I. Basbaum, unpublished observation.
54. M. Koltzenburg, C. L. Stucky, G. R. Lewin, *J. Neurophysiol.* **78**, 1841 (1997).
55. R. Doucette, E. Theriault, J. Diamond, *J. Comp. Neurol.* **261**, 583 (1987).
56. A. Guo, L. Vulchanova, J. Wang, X. Li, R. Elde, *Eur. J. Neurosci.* **11**, 946 (1999).
57. D. C. Yeomans, V. Pirec, H. K. Proudfit, *Pain* **68**, 133 (1996).
58. For supplemental data, see www.sciencemag.org/feature/data/1048712.shl.
59. Y. Q. Cao *et al.*, *Nature* **392**, 390 (1998).
60. We thank members of the Dallman lab for experimental advice and assistance and J. Poblete, L. Sun, G. Gerkoff, K. Schmidt, N. Kileen, and J. Meneses for expert technical advice and assistance. This work was supported by American Cancer Society and National Alliance for Research on Schizophrenia and Depression postdoctoral fellowships (M.J.C.), by NIH postdoctoral training grant NS07265 (W.J.M.), and by grants from Deutsche Forschungsgemeinschaft (SFB 353; M.K.), the National Institute of Neurological Disorders and Stroke, National Institute of Dental and Craniofacial Research, and the National Institute of Mental Health (D.J. and A.I.B.), and the Sandler Family Supporting Foundation (D.J.).

18 January 2000; accepted 9 March 2000

REPORTS

Titanium Carbide Nanocrystals in Circumstellar Environments

G. von Helden,[1,2]* A. G. G. M. Tielens,[3] D. van Heijnsbergen,[1,2] M. A. Duncan,[4] S. Hony,[5] L. B. F. M. Waters,[5,6] G. Meijer[1,2]

Meteorites contain micrometer-sized graphite grains with embedded titanium carbide grains. Although isotopic analysis identifies asymptotic giant branch stars as the birth sites of these grains, there is no direct observational identification of these grains in astronomical sources. We report that infrared wavelength spectra of gas-phase titanium carbide nanocrystals derived in the laboratory show a prominent feature at a wavelength of 20.1 micrometers, which compares well to a similar feature in observed spectra of postasymptotic giant branch stars. It is concluded that titanium carbide forms during a short (approximately 100 years) phase of catastrophic mass loss (>0.001 solar masses per year) in dying, low-mass stars.

Meteorites are known to contain micrometer-sized graphite grains whose isotopic composition suggests an origin in the ejecta of stars on the asymptotic giant branch (AGB), a late stage of evolution in the life of low-mass stars characterized by the nucleosynthesis of elemental C through the triple-α process and s-process elements in the star's interior (*1*). These newly synthesized elements are mixed to the surface, where they slowly turn the star into a C-rich object. These elements are eventually spread over the galaxy in a wind, much of it in the form of stardust. Analysis of individual stardust grains recovered from meteorites reveals internal TiC grains, often as cores which served as heterogeneous nucleation centers for graphite grain condensation (*2*). Although isotopic analysis pinpoints AGB stars as the formation sites for this stardust, there is no direct astronomical evidence for its origin from these objects. Moreover, the sizes and composition of these grains are not well understood in current models of dust formation on the AGB (*3*). We present astronomical evidence for the presence of TiC nanocrystals—and hence the graphitic stardust—in space, specifically near stars that are the evolutionary descendants of AGB stars.

AGB stars are a prime source of carbonaceous dust in the interstellar medium (*4*), and the composition, origin, and evolution of this dust has been studied through observations, particularly in the infrared (IR) wavelength range. These observations reveal the dominance of carbonaceous materials, such as

[1]FOM Institute for Plasma Physics Rijnhuizen, Edisonbaan 14, NL-3430 BE Nieuwegein, Netherlands. [2]Department of Molecular and Laser Physics, University of Nijmegen, Toernooiveld 1, NL-6525 ED Nijmegen, Netherlands. [3]SRON/Kapteyn Institute, University of Groningen, Landleven 12, NL-9700 AV Groningen, Netherlands. [4]Department of Chemistry, University of Georgia, Athens, GA 30602, USA. [5]Astronomical Institute, University of Amsterdam, Kruislaan 403, NL-1098 SJ Amsterdam, Netherlands. [6]Instituut voor Sterrenkunde, Katholieke Universiteit Leuven, Celestijnenlaan 200B, 3001 B-Heverlee, Belgium.

*To whom correspondence should be addressed. E-mail: gertvh@rijnh.nl

amorphous carbon, polycyclic aromatic hydrocarbon molecules (PAHs), and SiC, in stardust birth sites where the elemental abundance of C exceeds that of O (*5, 6*). In addition, a number of characteristic IR emission features have been recognized in the spectra of circumstellar dust, which have been used to search for specific classes of objects in the Infrared Astronomical Satellite (IRAS) spectral catalog (*7*). In particular, a feature near 21-μm wavelength, now known to be at 20.1 μm (*8*), has led to the identification of a class of sources known collectively as the "21-μm sources" (*9*). Optical spectroscopy has shown that these 21-μm sources are metal-poor, C-rich, red giants with stellar temperatures in the range of 5000 to 8000 K and enhanced s-process elemental abundances, supporting their post-AGB nature (*10–12*). These population II (*13*) stars with $M \sim 1\ M_{\odot}$ were formed during the early history of the Milky Way and have now, after some 10^{10} years, just reached the post-AGB phase, which is the last phase in the life of all low-mass stars.

We measured the IR and far-IR spectra for gas-phase metal carbide clusters (*14*) using the free electron laser for infrared experiments (FELIX) (*15*). For Ti_8C_{12} and $Ti_{14}C_{13}$, spectra provide evidence (*16*) for the previously proposed Met-Car (*17*) and nanocrystal (*18*) structures. A structural assignment based upon mass spectra for larger TiC clusters is complicated by the broad isotope distribution of Ti. The IR spectra of those larger clusters are, however, similar to that of $Ti_{14}C_{13}$, which indicates that the larger clusters have nanocrystalline structures. For each size of the TiC clusters in the experiments, the wavelength dependence of the ion signal was measured, but these IR spectra were indistinguishable. The wavelength spectra of the different nanocrystals with sizes ranging from 3 atoms by 3 atoms by 3 atoms (3×3×3 atoms) to 5×5×5 atoms were therefore summed (Fig. 1) to produce a composite spectrum, showing a strong peak near 20.1 μm with a width of about 1.8 μm.

We investigated the composition of dust in the surroundings of AGB stars, post-AGB objects, and planetary nebulae (PNe) using the short-wavelength spectrometer (SWS) (*19*) on board the IR space satellite (ISO) (*20*). Here, we concentrate on those objects that have a C-to-O elemental abundance ratio larger than unity and are therefore expected to form carbonaceous compounds. While these objects represent sequential stages in the evolution of low-mass stars—separated in age by typically less than 10,000 years—their IR emission is actually otherwise remarkably different. The IR spectra of post-AGB objects show strong and broad 8- and 12-μm features superimposed with weak PAH emission features. Most remarkably, however, the IR spectra of these sources are dominated by a distinct 20.1-μm feature, which in all sources has the same peak wavelength (20.1 μm) and profile (*8*). The spectrum of SAO 96709 (also known as HD 56126) shows the presence of a very strong 20.1-μm feature (Fig. 1). This feature is unique to the post-AGB phase of stellar evolution and has never been observed for objects in other evolutionary phases. The 20.1-μm feature does not correlate with any other spectral feature of these objects. Among the proposed identifications for the 20.1-μm emission feature are SiS_2 grains (*21, 22*), small diamonds (*23*), and urea molecules (*24*). However, in no case was the comparison with laboratory spectra compelling or the origin and evolution of the carrier in this particular class of objects clarified.

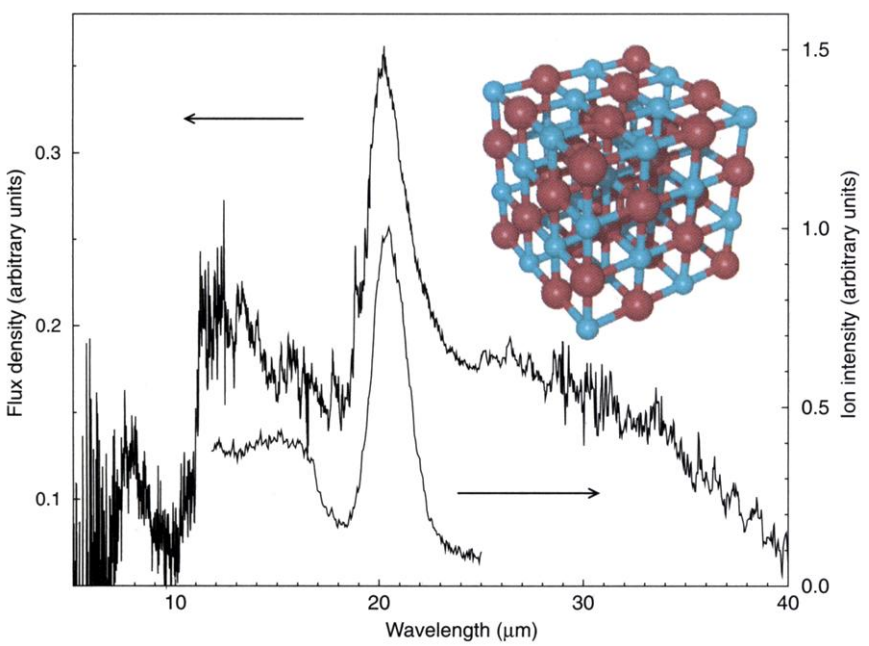

Fig. 1. The emission spectrum from the post-AGB object SAO 96709, taken by the ISO satellite (upper trace, left axis) and the wavelength spectra of TiC nanocrystal clusters recorded in the laboratory (lower trace, right axis). Also shown is a pictorial representation of a typical (4×4×4 atom) TiC nanocrystal. Carbon atoms are red; Ti atoms are blue.

Comparing the two spectra (Fig. 1), it is evident that the strong emission peak from the ISO observations of SAO 96709 agrees in position and width with the 20.1-μm peak in the IR spectrum of TiC clusters derived in the laboratory. In the laboratory, the profile is influenced by the dynamical process of light absorption while the cluster is being heated by the laser. Nonetheless, any shift or broadening in the laboratory spectrum cannot be much greater than the bandwidth of the excitation laser (≈0.1 μm full width at half maximum) and is thus small compared to the total width of the peaks in Fig. 1. In the laboratory experiments, the spectral structure is independent of the cluster size, at least in the range from 27 to 125 atoms. No experimental data on larger clusters is available, but the spectrum can be compared to that of bulk TiC. There, electron energy loss spectroscopy (EELS) shows the presence of a vibrational mode at almost the same position observed in the IR ionization study and the ISO spectrum (*25*). An emission peak of TiC nanocrystals can therefore be strong, because crystallites of all astrophysically relevant sizes have similar profiles and can contribute to its intensity.

The observed flux in the 20.1-μm feature can be converted to a total mass of TiC grains around these sources, using the calculated intrinsic strength of this band [600 km/mol for $Ti_{14}C_{13}$ (*26*); $= 7 \times 10^{-18}$ cm/Ti-atom]. The main uncertainty is in the adopted temperature. For both of the two best studied 21-μm objects, IRAS 22272 and IRAS 07134 (SAO 34504 and 96709, respectively), dust continuum temperatures of ≃190 and ≃80 K have been derived from the observed emission at 10 to 20 and 60 to 100 μm, respectively (*27, 28*). The emission temperature associated with the 20.1-μm carrier is not well constrained. Representing the 20.1-μm TiC band by a single oscillator, the Planck-mean absorption efficiency is calculated to be about 70 $cm^2\ g^{-1}$ for temperatures between 100 and 500 K. Given the observed total fluxes and sizes measured at a wavelength of 20 μm (*27, 28*) of IRAS 22272 and IRAS 07134, TiC temperatures of 475 and 265 K are calculated, independent of the distance (d) of these objects from Earth. For comparison, for 1-μm graphite grains, which emit efficiently over a wider wavelength range, we calculate a temperature of 120 and 75 K, and such grains may be responsible for the ob-

served continuum. The calculated TiC temperatures translate into Ti-masses of 10^{-7} $(d/1\text{kpc})^2$ and 9×10^{-7} $(d/1\text{kpc})^2$ $M_\odot$ (kpc = kiloparsec), for IRAS 22272 and IRAS 07134, respectively. Titanium is typically depleted in these metal-poor post-AGB objects by a factor of 2 to 10 compared to solar abundances (6.4×10^{-6} by mass) (*12*). Adopting a Ti abundance of 10^{-6} relative to H by mass, the total H mass of the envelopes is calculated to be 10^{-1} $(d/1\text{kpc})^2$ and 9×10^{-1} $(d/1\text{kpc})^2$ $M_\odot$, for IRAS 22272 and IRAS 07134, respectively. These dust estimates are consistent with those derived from modeling the spatial and spectral energy distribution of the continuum emission of these objects (*27, 28*). Thus, we conclude that the available Ti has been efficiently locked up in TiC grains in these sources. Moreover, all of this dust is still warm and close to the central star [$\sim 10^{16}$ $(d/1\text{kpc})$ cm (*27, 28*)] and has been ejected recently ($\simeq$500 year).

Our results have important implications for the understanding of the last stages of evolution of low-mass stars. The Ti abundance in low-mass stars is so low that high densities are required just to get a high enough collision rate for TiC grains to grow to the sizes observed in graphite stardust [$\sim$200 Å in diameter (*2*)]. For a typical expansion time scale of 100 days in the stellar ejecta, a pressure of 0.1 Pa is required. The pressure is also constrained by the requirement that the TiC has to condense before the graphite grains (in which the TiC will be trapped) form. For the observed C/O ratios in these objects—only slightly larger than unity (*12*)—this also implies pressures of the order of 0.1 Pa (*2*). These pressures are much higher than commonly adopted ($\sim 10^{-4}$ Pa) in theoretical models for nucleation and condensation of dust in AGB ejecta (*2, 29*). We conclude that the 20.1-μm feature of TiC is a signature of a phase of high density and high mass-loss rate. Astronomical observations reveal that the 21-μm feature is not observed in AGB stars, but rather only during a short-lived (<1000 years) phase directly after the AGB phase. Therefore, we conclude that these TiC nanocrystals are formed during the so-called superwind phase, which is a phase of high mass-loss where AGB stars lose the remaining stellar envelope, terminating their life on the AGB (*30*). Our analysis shows that the mass lost during this superwind phase represents a substantial fraction (~ 0.5 $M_\odot$) of the initial stellar mass. The physical processes responsible for the superwind phase are not well understood (*31*). However, given the metallicity pattern of these objects, this phase may coincide with a thermal pulse that dredges up newly synthesized material from the stellar interior and changes the star into a C-rich object. From the mass of TiC grains derived above, we conclude that ~ 0.5 $M_\odot$ is involved in this catastrophic event, and we derive a mass-loss rate exceeding 10^{-3} $M_\odot$/year. A similarly high mass-loss rate during the superwind has been derived from the observation of highly rotationally excited CO (*32*) for the so-called egg nebula—the only normal metallicity, post-AGB object with a 20.1-μm feature. Mid-IR studies of 21-μm objects reveal an axisymmetric structure for the emission, which implies an equator-to-pole density contrast of 20 (*27, 28*), further enhancing the densities at which dust condensation takes place. Examination of the stellar mass budget suggests that these objects cannot have lost much mass before this superwind phase. This may be related to the low metallicity of these objects, i.e., during the preceding phases (with C/O < 1), insufficient oxide or silicate dust could form to drive a large mass loss. Although the idea of a superwind terminating the AGB has been around for some 20 years (*30*), mass-loss rates estimated in the past for this event from observations of AGB objects (e.g., OH/IR stars, the pre-AGB-tip objects) are an order of magnitude less [10^{-4} $M_\odot$/year (*33*)]. Thus, the TiC identification suggests that rather than with a wimpy wind, low-mass stars end their life with (almost) a bang.

In the different sources, the 21-μm feature represents between 3×10^{-3} and 3×10^{-2} of the total stellar luminosity. Most of the emission comes out in the mid- and far-IR continuum carried by large graphite or amorphous carbon particles (*27, 28*). This 20.1-μm feature-to-continuum ratio is higher than might be expected from the Ti/C abundance ratio ($\simeq 1.5 \times 10^{-3}$ by mass) in this class of objects (*12*). We attribute this high ratio to the small size of the TiC nanocrystals. From abundance considerations, we expect graphite grains to grow to much larger sizes than TiC grains, and such large grains are poor absorbers of stellar light on a per mass basis. Although there is no direct information on the sizes of the grains around these objects, meteoritic graphite grains have diameters in the range of 0.3 to 9 μm, whereas the embedded TiC grains are $\simeq$0.02 μm in diameter. There is no sign of the 20.1-μm feature in the IR spectra of PNe, which is the subsequent evolutionary phase of AGB stars, or in the interstellar medium. In general, there is a strong spectral evolution in the IR from the AGB through the post-AGB to the PNe phase, reflecting destruction of the emitting dust (*34*). Only the largest grains and their inclusions may survive this process to be eventually incorporated into the solar system.

Our laboratory studies also have implications for models of dust nucleation and condensation in stellar ejecta. As in the laboratory, stable cluster intermediaries may play an important role in the condensation of TiC dust in astrophysical settings (*35*). We suggest that the sequence from the 3×3×3 to the 5×5×5 atom clusters may well be the first steps for this process. Furthermore, we emphasize that thermal electron emission may be essential in the formation of such small clusters. When a growing cluster undergoes a collision with either a C or a transition metal atom, the binding energy of this atom has to be released from the collision complex. In low-density environments, this usually happens by radiative relaxation. This process is, however, not very efficient, and the transient collision complex will usually dissociate back to reactants. In species that can undergo thermal electron emission, on the other hand, an electron can be emitted instead. The resulting ion is now stable toward dissociation, and it can frequently recapture a free electron, each time having the opportunity to radiatively cool itself. In a similar vein, when a nanocrystal is excited by an ultraviolet photon or an energetic particle, instead of dissociation, an electron can be emitted, taking away energy.

References and Notes

1. E. Anders and E. Zinner, *Meteoritics* **28**, 490 (1993).
2. T. J. Bernatowicz *et al.*, *Astrophys. J.* **472**, 760 (1996).
3. M. Jura, *AIP Conf. Proc.* **402**, 379 (1997).
4. A. G. G. M. Tielens, in *Formation and Evolution of Solids in Space*, J. M. Greenberg and A. Li, Eds. (Kluwer, Dordrecht, Netherlands, 1999), pp. 331–375.
5. A series of articles in *The Universe as Seen by ISO*, P. Cox and M. F. Kessler, Eds., ESA SP-427 (ESA Publications, Division, Noordwijk, Netherlands, 1999).
6. F. J. Molster *et al.*, *Astron. Astrophys.* **315**, L373 (1996).
7. M. Jourdain de Muizon, in *Infrared Astronomy with ISO*, Th. Encrenaz and M. F. Kessler, Eds. (Nova Science, New York, 1992), p. 489.
8. K. Volk, S. Kwok, B. J. Hrivnak, *Astrophys. J.* **516**, L99 (1999).
9. S. Kwok, K. Volk, B. J. Hrivnak, *Astrophys. J.* **345**, L51 (1989).
10. B. J. Hrivnak, *Astrophys. J.* **438**, 341 (1995).
11. H. van Winckel, in *Asymptotic Giant Branch Stars*, T. Le Bertre, A. Lèbre, C. Waelkens, Eds. (Astronomical Society of the Pacific, San Francisco, CA, 1999), p. 465.
12. H. van Winckel and M. Reyniers, *Astron. Astrophys.* **354**, 135 (2000).
13. Because of their metallicity, kinematics, and spatial distribution, population II stars are thought to be older stars formed early on in the formation of the Milky Way.
14. These experiments use the new technique of infrared laser induced thermal ionization with a free-electron laser. Neutral clusters are irradiated by a pulsed IR laser. When the laser wavelength is resonant with an IR active mode, the cluster can be heated by multiple absorption of photons. When there is sufficient excess energy, dissociation may occur. However, in clusters with strong bonding and a relatively low ionization energy, as is the case for some metal-carbide clusters, electron emission can become competitive with, or even dominant over, dissociation. Tuning the laser while measuring the mass-analyzed ion yield produces an IR spectrum of the neutral cluster.
15. D. Oepts, A. F. G. van der Meer, P. W. van Amersfoort, *Infrared Phys. Technol.* **36**, 297 (1995).
16. D. van Heijnsbergen, G. von Helden, M. A. Duncan, A. J. A. van Roij, G. Meijer, *Phys. Rev. Lett.* **83**, 4983 (1999).
17. B. C. Guo, K. P. Kerns, A. W. Castleman Jr., *Science* **255**, 1411 (1992).
18. J. S. Pilgrim and M. A. Duncan, *J. Am. Chem. Soc.* **115**, 9724 (1993).

19. Th. de Graauw *et al.*, *Astron. Astrophys.* **315**, L49 (1996).
20. Based on ISO, European Space Agency (ESA) project with instruments funded by ESA Member States (especially the principal investigator countries: France, Germany, the Netherlands, and the United Kingdom) and with participation of ISAS and NASA.
21. J. Goebel, *Astron. Astrophys.* **278**, 226 (1993).
22. B. Begemann, J. Dorschner, Th. Henning, H. Mutschke, *Astrophys. J.* **464**, L195 (1996).
23. H. M. Hill, A. P. Jones, L. d'Hendecourt, *Astron. Astrophys.* **336**, L41 (1998).
24. C. Souriseau, G. Coddens, R. Papoular, *Astron. Astrophys.* **254**, L1 (1992).
25. C. Oshima *et al.*, *Phys. Rev. B* **36**, 7510 (1987).
26. I. Dance, personal communication.
27. A. Dayal *et al.*, *Astrophys. J.* **492**, 603 (1998).
28. M. Meixner *et al.*, *Astrophys. J.* **482**, 897, (1996)
29. S. Höfner, U. G. Jorgensen, R. Loidl, B. Aringer, *Astron. Astrophys.* **340**, 497 (1998).
30. A. Renzini, in *Physical Processes in Red Giants*, I. Iben and A. Renzini, Eds. (Reidel, Dordrecht, Netherlands, 1981), pp. 431–446.
31. E. Vassiliadis and P. R. Wood, *Astrophys. J.* **413**, 641 (1993).
32. K. Justtanont, A. G. G. M. Tielens, C. J. Skinner, M. R. Haas, *Astrophys. J.* **476**, 319 (1996).
33. K. Justtanont and A. G. G. M. Tielens, *Astrophys. J.* **389**, 400 (1992).
34. R. H. Buss *et al.*, *Astrophys. J.* **415**, 250 (1993).
35. I. Cherchneff and P. Cau, in *Asymptotic Giant Branch Stars*, T. Le Bertre, A. Lèbre, C. Waelkens, Eds. (Astronomical Society of the Pacific San Francisco, CA, 1999), p. 251.
36. We greatly appreciate the skillful assistance of the FELIX staff in providing the required beam time on FELIX. This work is part of the research program of the Stichting voor Fundamenteel Onderzoek der Materie (FOM), which is supported financially by the Nederlandse Organisatie voor Wetenschappelijk Onderzoek (NWO) and receives direct support from the NWO via PIONIER-grant 030-66-089. M.A.D. acknowledges support from the U.S. Air Force Office of Scientific Research grant F49620-97-1-0042. L.B.F.M.W. acknowledges support from NWO through PIONIER-grant 616-78-333

19 January 2000; accepted 13 March 2000

Translating Biomolecular Recognition into Nanomechanics

J. Fritz,[1,2] M. K. Baller,[1,2] H. P. Lang,[1,2] H. Rothuizen,[1] P. Vettiger,[1] E. Meyer,[2] H.-J. Güntherodt,[2] Ch. Gerber,[1]* J. K. Gimzewski[1]

We report the specific transduction, via surface stress changes, of DNA hybridization and receptor-ligand binding into a direct nanomechanical response of microfabricated cantilevers. Cantilevers in an array were functionalized with a selection of biomolecules. The differential deflection of the cantilevers was found to provide a true molecular recognition signal despite large nonspecific responses of individual cantilevers. Hybridization of complementary oligonucleotides shows that a single base mismatch between two 12-mer oligonucleotides is clearly detectable. Similar experiments on protein A–immunoglobulin interactions demonstrate the wide-ranging applicability of nanomechanical transduction to detect biomolecular recognition.

In recent years, biomolecules and their unique ability of molecular recognition have been investigated in terms of their mechanical response to external forces. A common feature of methods such as atomic force microscopy (AFM) (*1–3*), optical tweezers (*4*), and magnetic bead experiments (*5*) is that the molecules are probed by applying an external force. Conversely, intermolecular forces arising from adsorption of small molecules are known to induce surface stress, directly resulting in the mechanical bending of a solid surface or a cantilever (*6–9*). Recently, cantilever bending by nonspecific adsorption of proteins was reported (*10, 11*). An analogous transduction process is found in biology, where the interaction of membrane molecules modifies the lateral tension of a lipid bilayer. The resulting curvature of the membrane is responsible for mechanically triggering membrane protein function (*12*).

We have taken advantage of biochemically induced surface stress to directly and specifically transduce molecular recognition into nanomechanical responses in a cantilever array. This is achieved by immobilizing a monolayer of receptor molecules on one side of the cantilevers and then detecting the mechanical bending induced by ligand binding in a liquid environment. A major advantage of such a direct transduction is that it eliminates the requirement that the molecules under investigation be labeled, for example, with fluorescence or radioactive tags.

DNA hybridization is a prominent example of molecular recognition, fundamental to the biological processes of replication, transcription, and translation. Consequently, we studied the surface stress arising from Watson–Crick base pairing between unlabeled oligonucleotides and their surface-immobilized binding partners. Hybridization experiments were performed in a liquid cell containing a silicon cantilever array immersed in hybridization buffer (Fig. 1) (*13*). The bending of each cantilever was measured in situ, using an optical beam deflection technique (*14*). Synthetic 5′ thio-modified oligonucleotides with different base sequences were covalently immobilized on the gold-covered side of the cantilevers (Fig. 2A) (*15*). The functionalization of one cantilever with a 12-mer oligonucleotide and the other with a 16-mer oligonucleotide was performed in parallel under identical conditions (*15*). The arrays were equilibrated in hybridization buffer until the differential signal became stable. Then, the complementary 16-mer oligonucleotide solution was injected into the liquid cell (Fig. 2B) followed by injection of complementary 12-mer oligonucleotide solution (Fig. 2C). The injections lead to hybridization of oligonucleotides in solution with the matching oligonucleotides immobilized on the cantilever surfaces. This results in a difference in surface stress between the functionalized gold and the nonfunctionalized Si surface, which bends the cantilever. During the entire process, the absolute deflections of individual cantilevers were recorded (Fig. 3A). Simultaneously, we extracted the differential signal (deflection of cantilever covered by the 16-mer oligonucletoide minus deflection of the cantilever covered by the 12-mer oligonucelotide) (Fig. 3B).

Signals from individual cantilevers displayed drifts of several tens of nm during equilibration (interval I in Fig. 3A). In general, injections of liquid resulted in spikes of up to 100 nm in amplitude, which are ascribable to turbulences. This was followed by an immediate increase of the signal by ~50 nm

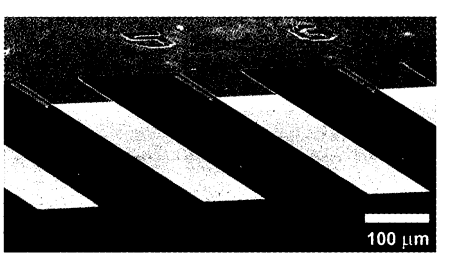

Fig. 1. Scanning electron micrograph of a section of a microfabricated silicon cantilever array (eight cantilevers, each 1 μm thick, 500 μm long, and 100 μm wide, with a pitch of 250 μm, spring constant 0.02 N m^{-1}; Micro- and Nanomechanics Group, IBM Zurich Research Laboratory, Switzerland).

[1]IBM Research, Zurich Research Laboratory, Säumerstrasse 4, CH-8803 Rüschlikon, Switzerland. [2]Physics Institute, University of Basel, Klingelbergstrasse 82, CH-4056 Basel, Switzerland.

*To whom correspondence should be addressed. E-mail: ge@zurich.ibm.com